Topological nodal-line semimetal in nonsymmorphic *Cmce*-phase Ag$_2$S

Huaqing Huang,[1] Kyung-Hwan Jin,[1] and Feng Liu[1,2,*]

[1]*Department of Materials Science and Engineering, University of Utah, Salt Lake City, Utah 84112, USA*
[2]*Collaborative Innovation Center of Quantum Matter, Beijing 100084, China*

Based on first-principles calculations and symmetry analysis, we discovery that the Ag$_2$S with *Cmce* symmetry is a topological nodal-line semimetal in the absence of spin-orbit coupling. A single nodal loop as protected by the glide symmetry exists around the center of the Brillouin zone, dispersing slightly in the momentum space to form both electron and hole pockets around the loop. Moreover, a nearly flat drumheadlike surface state appears on the (001) surface of this material. The nodal-line semimetal phase and its drumheadlike surface states are expected to be experimentally detectable in *Cmce*-phase Ag$_2$S because spin-orbit coupling will only open a negligible gap comparing to the energy dispersion of the nodal loop. Our finding provides a different member to the growing family of nodal-line semimetals with a single nodal loop structure.

I. INTRODUCTION

Recently, topological nodal-line systems characterized by one-dimensional (1D) lines of band crossing around the Fermi level have attracted intense interest. Due to different structures (number, distribution, and connection) of nodal lines in momentum space, they can be classified into different groups, for instance, simple nodal-line semimetals [1–4], nodal chain metals [5], nodal net semimetals [6–8], nodal-link semimetals [9–11], and nodal-knot semimetals [12]. Consequently, nodal-line systems show various exotic physical properties, such as topological protected flat drumheadlike surface states [1–12], giant surface Friedel oscillation [13,14], special collective mode [14,15], large intrinsic spin Hall effects [16], flat Landau level [17], anisotropic optical conductivity [18,19], long-range Coulomb interaction [20], and correlation phenomena [21]. For all nodal-line systems, the basic building block of their complicated nodal-line structures is a single nodal loop. Hence, finding a real material with only one nodal loop would provide a useful starting base system to investigate nodal-line related physics and understand novel physical properties of other systems with complicated nodal-line structures. Although there are few single nodal loop systems known to date [22–27], some of them require complicated crystal structures or external pressures and may have extra bands around the Fermi level.

Ag$_2$S belongs to a large family of silver chalcogenides Ag$_2$E (E = S, Se, and Te), which have different allotropes [28,29]. The low-temperature semiconducting monocliinc β phase of Ag$_2$S is known as an acanthite mineral in nature, which is an important ore of silver. Other β-phase silver chalcogenides exhibit interesting properties, such as large and nonsaturating linear magnetoresistance [30] and a three-dimensional (3D) topological insulating state [31]. As temperature increases, Ag$_2$S undergoes phase transitions into the body-centered-cubic α phase (the so-called argentite) at 453 K or the face-centered-cubic γ phase at 859 K, which are electrical conductors [32,33]. In addition to these phases of silver chalcogenides, recently several new allotropes have been theoretically or experimentally discovered [34–37]

expanding rich physical properties and potential applications in the family of silver chalcogenides.

In this paper, we discover a topological nodal-line semimetal state in an allotrope of Ag$_2$S with the nonsymmorphic *Cmce* symmetry when spin-orbit coupling (SOC) is absent. Unlike other nodal-line semimetals with multiple nodal lines forming complicated nodal-line structures, this system exhibits a single glide symmetry-protected nodal loop on the k_x-k_y plane, which provides a good base system to study those properties solely induced by one nodal loop. When the nodal loop is projected onto the (001) surface to form a circle, a nearly flat drumheadlike surface band nestled inside of the projected nodal circle is formed. When SOC is included, the nodal loop is gapped slightly, and the system becomes a topological semimetal [38] with $\mathbb{Z}_2$ topological invariant (1, 000). Because the SOC-induced splitting is quite small comparing to the energy dispersion of the nodal loop, the nodal-line semimetal and its exotic physical properties still are expected to be observed in this allotrope of silver sulfide.

II. CRYSTAL STRUCTURE AND METHODS

Although there are different allotropes of silver sulfide, here we focus on the Ag$_2$S which crystallizes in the orthorhombic crystal structure with the nonsymmorphic space-group *Cmce* (D_{2h}^{18}, No. 64) [39]. The calculated total energy of the *Cmce*-Ag$_2$S is just tens to few hundreds of millielectron volts higher than that of other allotropes, indicating that the *Cmce* phase of Ag$_2$S is metastable but energetically accessible. The conventional cell and the primitive cell of Ag$_2$S are shown in Figs. 1(a) and 1(b), respectively. In this structure, the Ag atoms lie on the mirror plane (M_{100}), which is perpendicular to the twofold rotation axis ($C_{2(100)}$), whereas S atoms occupy the inversion centers [(0,0,0) and ($\frac{1}{2}$,$\frac{1}{2}$,0)]. In addition to point-group symmetry operations, the nonsymmorphic space-group *Cmce* of this structure also contains several compound symmetry operations of glide planes and screw axes (see Table I). One of the most important symmetries, the glide plane $\tilde{M}_{001} = \{M_{001}|0,\frac{1}{2},\frac{1}{2}\}$, which is related directly to the existence of nodal loop in Ag$_2$S, consists of a fractional translation $\tau = (0,\frac{1}{2},\frac{1}{2})$ followed by a mirror reflection M_{001}.
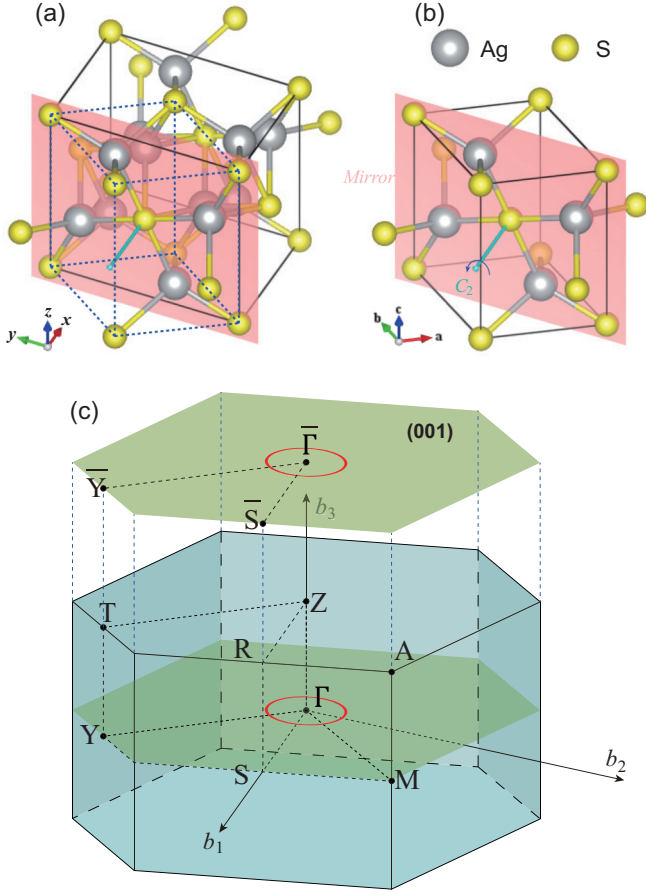
FIG. 1. Crystal structure of Ag$_2$S with *Cmce* (No. 64) symmetry in (a) a conventional cell and (b) an orthorhombic primitive cell. The semitransparent red plane indicates a mirror plane (M_{100}), and the light green arrow indicates a twofold rotation axis ($C_{2(100)}$). (c) The bulk Brillouin zone and the projected surface Brillouin zone of the (001) plane.

To explore the electronic properties of Ag$_2$S, we perform first-principles calculations within the framework of density-functional theory using the Perdew-Burke-Ernzerhof-type [40] generalized gradient approximation for the exchange-correlation functional as implemented in the Vienna *ab initio* simulation package [41]. An $18 \times 18 \times 12$ grid of **k** points

TABLE I. Symmetries of Ag$_2$S with the nonsymmorphic space-group *Cmce* (No. 64).

Symmetry	(x,y,z) form	Operation
Identify	(x,y,z)	$\{1\vert 0\}$
Inversion	$(-x,-y,-z)$	$\{-1\vert 0\}$
Screw axis	$(-x,-y+\frac{1}{2},z+\frac{1}{2})$	$\{C_{2(001)}\vert 0,\frac{1}{2},\frac{1}{2}\}$
Screw axis	$(-x,y+\frac{1}{2},-z+\frac{1}{2})$	$\{C_{2(010)}\vert 0,\frac{1}{2},\frac{1}{2}\}$
Rotation	$(x,-y,-z)$	$C_{2(100)}$
Glide plane	$(x,y+\frac{1}{2},-z+\frac{1}{2})$	$\{M_{001}\vert 0,\frac{1}{2},\frac{1}{2}\}$
Glide plane	$(x,-y+\frac{1}{2},z+\frac{1}{2})$	$\{M_{010}\vert 0,\frac{1}{2},\frac{1}{2}\}$
Mirror	$(-x,y,z)$	M_{100}

and a default plane-wave energy cutoff are adopted for the self-consistent field calculations. The electronic structures are calculated both with and without SOC. We construct Wannier representations [42,43] by projecting the Bloch states from the first-principles calculations of bulk materials onto Ag s, d, and S p orbitals without an iterative maximal-localization procedure [44–46]. Based on Wannier representations, we further calculate the surface density of states and the surface-projected Fermi surface using the iterative Green's function method for the (001) surface of a semi-infinite system [47–50].

III. RESULTS AND DISCUSSION

A. Electronic structures

We first study the band structure of *Cmce*-phase Ag$_2$S in the absence of SOC. As shown in Fig. 2, the conduction and valence bands are inverted around the Γ point and cross each other along the Y-Γ and Γ-S lines near the Fermi level which gives rise to nontrivial band topology of Ag$_2$S. Without SOC, the eigenvalues of the glide symmetry $\widetilde{M}_{001} = \{M_{001}\vert 0,\frac{1}{2},\frac{1}{2}\}$ are given by $g_{\pm}(\mathbf{k}) = m_{\pm}\phi(\mathbf{k}) = \pm e^{ik_y/2}$, where $m_{\pm} = \pm 1$ is the spinless eigenvalues of mirror reflection symmetry M_{001} and $\phi(\mathbf{k}) = e^{ik_y/2}$ is the phase factor induced by the fractional translation. Since the lowest conduction band and the highest valence band have opposite signs of eigenvalues with respect to the glide symmetry $\widetilde{M}_{001}$, the band crossings between these two bands do not just appear at two isolated points on the Y-Γ and Γ-S lines [as shown in Fig. 2(a)] but actually form a continuous circlelike nodal loop around the Γ point on the Y-Γ-S plane. To reveal the energy dispersion of the nodal loop,
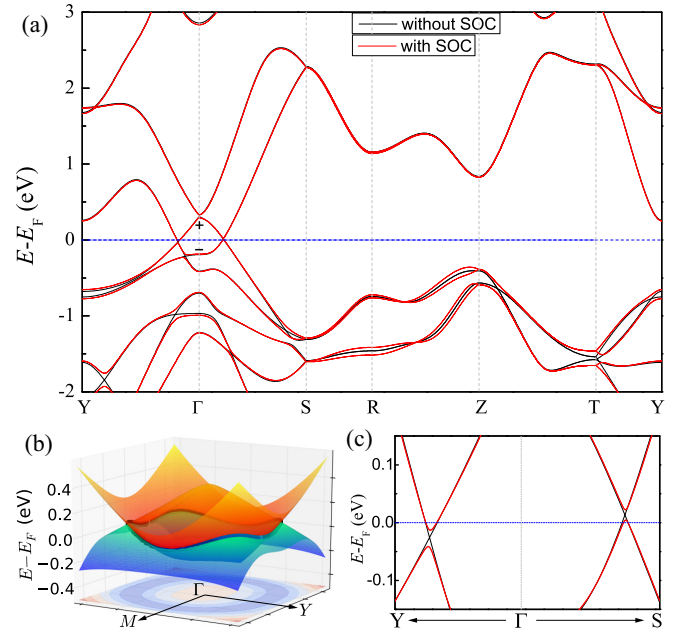

FIG. 2. (a) Band structure of *Cmce*-phase Ag$_2$S. The Fermi-level E_F is set to zero. The parities of states near the Fermi level at Γ are labeled with "+" or "−". (b) The three-dimensional plot of the band structure around the Fermi level. The bottom projection shows the isoenergy contour of the energy difference between the conduction and the valence bands. (c) The zoom-in plot of the band crossings around Γ near the Fermi level.
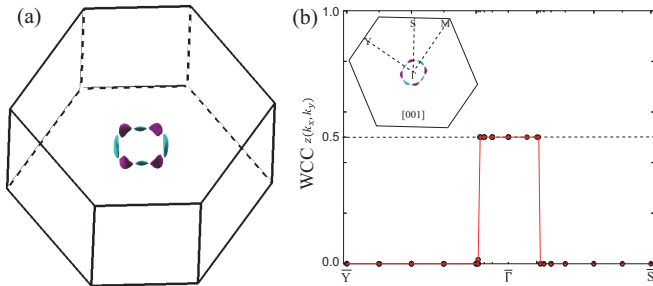
FIG. 3. (a) Three-dimensional Fermi surface of *Cmce*-phase Ag$_2$S where the green and purple colors represent electron and hole pockets, respectively. The electron and hole pockets contact at four points which are nodal points in the nodal loop. (b) Evolution of Wanner charge center $z(k_x,k_y)$ for the occupied bands.

we calculate the 3D band structure around the Γ point near the Fermi level. As shown in Fig. 2(b), the energy of the nodes in the loop varies within the range of -50 to $+50$ meV along the loop, making it quite flat in energy and momentum space.

The shape of the nodal loop can be inferred easily by looking at the Fermi surface of Ag$_2$S. As shown in Fig. 3, there are four electron and hole pockets each, connecting together to form a crownlike Fermi surface. The Fermi surface which encloses the nodal loop winds around the Γ point and takes the shape of a thin pipe (torus) with a varying radius. The nodal loop is cut by the Fermi-level E_F at eight points, each being a contacting point for electron and hole pockets. Comparing to other nodal-line semimetals with multiple nodal lines, *Cmce*-phase Ag$_2$S is a good base system to study nodal-line physics in the sense that it has only a simple nodal loop and the energy variation along the loop is small. Moreover, the Fermi surface is contributed mainly by the single nodal loop without other bands, which makes it easier to investigate novel properties directly related to the presence of the nodal loop. Projected onto the (001) surface, the nodal loop encloses a circular "patch" surrounding $\bar{\Gamma}$ within which topologically required surface states reside [Fig. 1(b)]. The area of the projected circular patch is found to be as large as 8% of the whole projected surface Brillouin zone in *Cmce*-phase Ag$_2$S [see the inset of Fig. 3(b)], which makes it easier to observe the nodal loop in the bulk as well as the nontrivial surface state by angle-resolved photoemission spectroscopy.

B. Evolution of Wannier charge centers

To identify nontrivial topology of electronic structures in Ag$_2$S, we investigate the evolution of 1D hybrid Wannier charge centers (WCCs) along the high-symmetry path of the k_x-k_y plane [51–54]. The 1D hybrid Wannier functions belonging to unit-cell $\mathbf{R}_z$ are constructed as

$$\left| W_{n\mathbf{R}_z}(k_x,k_y)\right\rangle = \frac{1}{2\pi}\int_0^{2\pi} dk_z e^{i\mathbf{k}\cdot(\mathbf{r}-\mathbf{R}_z)}|u_{n,\mathbf{k}}\rangle. \quad (1)$$

The WCC is defined as the expectation value $z_n(k_x,k_y) = \langle W_{n0}|\hat{z}|W_{n0}\rangle$ of the position operator $\hat{z}$ for the hybrid Wannier function in the "home" unit-cell $\mathbf{R}_z = 0$. The sum $z(k_x,k_y) = \sum_n z_n(k_x,k_y)$ over occupied bands gives a simple and direct way to comprehend the topology of the whole occupied
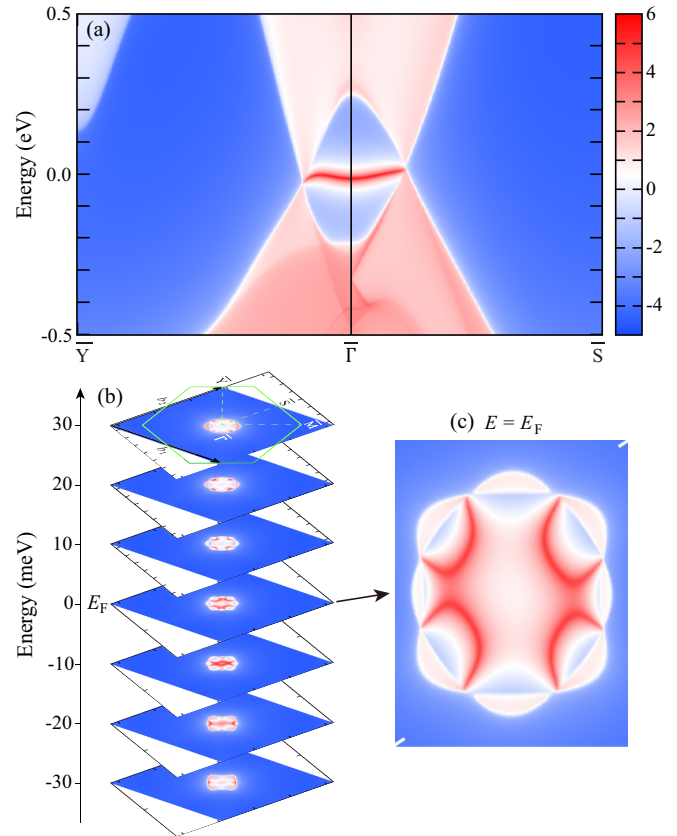

FIG. 4. The projected surface states and isoenergy surface for the (001) surface of *Cmce*-phase Ag$_2$S. (a) The projected surface density of states for the (001) surface where a flat surface band connecting two projections of nodal points is clearly visible. (b) The stacking plot of constant energy contours of the (001) surface. (c) The zoom-in isoenergy surfaces around $\bar{\Gamma}$ at the Fermi-level E_F.

subspace. As shown in Fig. 3(b), the $z(k_x,k_y) = 1/2$ within the projected nodal loop on the k_x-k_y plane around the Γ point, whereas $z(k_x,k_y)$ jumps to 0 when passing through the projected nodal loop to the outside. The total hybrid WCC $z(k_x,k_y)$ is equivalent to the Berry phase $\phi_B = \oint_C \mathcal{A}(\mathbf{k}) \cdot d\mathbf{k}$, where $\mathcal{A}(\mathbf{k}) = -i\sum_n\langle u_n(\mathbf{k})|\nabla_\mathbf{k} u_n(\mathbf{k})\rangle$ is the Berry connection of the occupied states and C is a circular (closed) path along the k_z direction subject to the periodicity of the Brillouin zone. In fact, this integral can be generalized to any arbitrary closed path C in momentum space. If path C encloses the nodal line, one has a Berry phase of $\phi_B = \pi$; otherwise, $\phi_B = 0$.

C. Drumheadlike surface states

According to the bulk-boundary correspondence, the so-called drumheadlike surface states are expected to appear on the top surface of *Cmce*-phase Ag$_2$S. As shown in Fig. 4(a), the surface states connect two gapless Dirac points, which are the projection of the nodal points. Interestingly, the drumheadlike surface states are nearly flat with small dispersion. Such two-dimensional flat bands indicate a high density of states around the Fermi level and partially filled occupation, providing a unique venue for strong-correlation and high-temperature superconductivity physics [55–58]. Because the nodal loop

exists on the k_x-k_y plane in the bulk Brillouin zone, the nodal loop projection onto the (001) surface shows a closed ring surrounding $\bar{\Gamma}$ [see Fig. 1(c) and the inset of Fig. 3(b)]. It is worth noting that the surface states are nestled in the projected interior of the closed nodal ring [see Figs. 4(b) and 4(c)], namely, it is a drumheadlike state. In particular, as the nodal loop is cut by E_F at eight nodal points, there are four pieces of Fermi arcs, each connects a pair of the projected nodal points [see Fig. 4(c)]. This drumheadlike surface state serves as direct evidence for the nodal-line semimetal state in $Cmce$-phase Ag_2S, which should be experimentally detectable by angle-resolved photoemission spectroscopy measurement.

D. Effect of spin-orbit coupling

The SOC effect can induce diverse topological phases in 3D nodal-line semimetals, including topological insulators [54,59,60], Dirac semimetals [7,8], and other kinds of nodal-line semimetals [61–63]. Analogous to graphene, SOC can gap out degenerate points along the nodal loop and drives the system into a topological semimetallic phase with nontrivial $\mathbb{Z}_2$ topology [38]. We calculate the topological invariant according to the evolution of the WCCs of the occupied Bloch states [52] and find $\mathbb{Z}_2 = (1, 000)$, signifying a nontrivial band topology. As shown in Fig. 2, although SOC will split other degenerate bands below the Fermi level significantly, the SOC-induced gap along the nodal loop turns out to be quite small [see Fig. 2(c)]. Further finer electronic structure calculations using Wannier interpolation indicate that SOC indeed opens tiny gaps along the nodal loop (with the maximum size of 28 meV on the Y-Γ line), which is much smaller than the dispersion of the nodal loop. The drumheadlike surface state

also splits slightly and becomes a Dirac surface state with small dispersion. Moreover, the SOC-induced splitting can be diminished by doping or substituting lighter elements with weak atomic SOC strength. We thus expect both the nodal-line semimetal and the nearly flat drumheadlike surface state should be experimentally accessible in the Ag_2S system.

IV. CONCLUSION

In conclusion, we discover that the $Cmce$-phase Ag_2S is a 3D topological nodal-line semimetal when SOC is absent. The $Cmce$-phase Ag_2S exhibits a single nodal loop in the bulk and a nearly flat drumheadlike surface state in the (001) surface. When SOC is included, the nodal loop is slightly gapped, and the system becomes a topological semimetallic state with nontrivial $\mathbb{Z}_2$ topology [38]. As the SOC-induced gap is small comparing to the energy variation of nodes along the loop, the nodal-line semimetal phase and its drumheadlike surface states are experimentally accessible in this material. With a simple nodal-line structure, the $Cmce$-phase Ag_2S provides an alternative route for studying nodal-line physics and understanding intriguing phenomena of other nodal-line systems with complicated nodal-line structures.

ACKNOWLEDGMENTS

[1] A. A. Burkov, M. D. Hook, and L. Balents, Phys. Rev. B **84**, 235126 (2011).

[2] M. Phillips and V. Aji, Phys. Rev. B **90**, 115111 (2014).

[3] C. Fang, H. Weng, X. Dai, and Z. Fang, Chin. Phys. B **25**, 117106 (2016).

[4] R. Yu, Z. Fang, X. Dai, and H. Weng, Front. Phys. **12**, 127202 (2017).

[5] T. Bzdušek, Q. Wu, A. Rüegg, M. Sigrist, and A. A. Soluyanov, Nature (London) **538**, 75 (2016).

[6] X. Feng, C. Yue, Z. Song, Q. Wu, and B. Wen, arXiv:1705.00511.

[7] Y. Kim, B. J. Wieder, C. L. Kane, and A. M. Rappe, Phys. Rev. Lett. **115**, 036806 (2015).

[8] R. Yu, H. Weng, Z. Fang, X. Dai, and X. Hu, Phys. Rev. Lett. **115**, 036807 (2015).

[9] Z. Yan, R. Bi, H. Shen, L. Lu, S.-C. Zhang, and Z. Wang, Phys. Rev. B **96**, 041103 (2017).

[10] P.-Y. Chang and C.-H. Yee, Phys. Rev. B **96**, 081114(R) (2017).

[11] W. Chen, H.-Z. Lu, and J.-M. Hou, Phys. Rev. B **96**, 041102 (2017).

[12] R. Bi, Z. Yan, L. Lu, and Z. Wang, arXiv:1704.06849.

[13] R. Li, H. Ma, X. Cheng, S. Wang, D. Li, Z. Zhang, Y. Li, and X.-Q. Chen, Phys. Rev. Lett. **117**, 096401 (2016).

[14] J.-W. Rhim and Y. B. Kim, New J. Phys. **18**, 043010 (2016).

[15] Z. Yan, P.-W. Huang, and Z. Wang, Phys. Rev. B **93**, 085138 (2016).

[16] Y. Sun, Y. Zhang, C.-X. Liu, C. Felser, and B. Yan, Phys. Rev. B **95**, 235104 (2017).

[17] J.-W. Rhim and Y. B. Kim, Phys. Rev. B **92**, 045126 (2015).

[18] S. Barati and S. H. Abedinpour, arXiv:1705.02243.

[19] S. Ahn, E. Mele, and H. Min, arXiv:1703.00130.

[20] Y. Huh, E.-G. Moon, and Y. B. Kim, Phys. Rev. B **93**, 035138 (2016).

[21] J. Liu and L. Balents, Phys. Rev. B **95**, 075426 (2017).

[22] Y.-H. Chan, C.-K. Chiu, M. Y. Chou, and A. P. Schnyder, Phys. Rev. B **93**, 205132 (2016); L. S. Xie, L. M. Schoop, E. M. Seibel, Q. D. Gibson, W. Xie, and R. J. Cava, APL Mater. **3**, 083602 (2015).

[23] H. Weng, Y. Liang, Q. Xu, R. Yu, Z. Fang, X. Dai, and Y. Kawazoe, Phys. Rev. B **92**, 045108 (2015).

[24] J.-T. Wang, H. Weng, S. Nie, Z. Fang, Y. Kawazoe, and C. Chen, Phys. Rev. Lett. **116**, 195501 (2016).

[25] Y. Chen, Y. Xie, S. A. Yang, H. Pan, F. Zhang, M. L. Cohen, and S. Zhang, Nano Lett. **15**, 6974 (2015).

[26] J. Zhao, R. Yu, H. Weng, and Z. Fang, Phys. Rev. B **94**, 195104 (2016).

[27] Q. Xu, R. Yu, Z. Fang, X. Dai, and H. Weng, Phys. Rev. B **95**, 045136 (2017); Y. Quan, Z. P. Yin, and W. E. Pickett, Phys. Rev. Lett. **118**, 176402 (2017).

[28] A. J. Frueh, Z. Kristallogr. **110**, 136 (1958).

[29] M. Kobayashi, Solid State Ionics **39**, 121 (1990).

[30] R. Xu, A. Husmann, T. Rosenbaum, M.-L. Saboungi, J. Enderby, and P. Littlewood, Nature (London) **390**, 57 (1997).

[31] W. Zhang, R. Yu, W. Feng, Y. Yao, H. Weng, X. Dai, and Z. Fang, Phys. Rev. Lett. **106**, 156808 (2011).

[32] R. Cava, F. Reidinger, and B. Wuensch, J. Solid State Chem. **31**, 69 (1980).

[33] B. H. Grier, S. M. Shapiro, and R. J. Cava, Phys. Rev. B **29**, 3810 (1984).

[34] D. Santamaría-Pérez, M. Marqués, R. Chuliá-Jordán, J. M. Menendez, O. Gomis, J. Ruiz-Fuertes, J. A. Sans, D. Errandonea, and J. M. Recio, Inorg. Chem. **51**, 5289 (2012).

[35] Z. Zhao, S. Wang, H. Zhang, and W. L. Mao, Phys. Rev. B **88**, 024120 (2013).

[36] Z. Zhao, S. Wang, A. R. Oganov, P. Chen, Z. Liu, and W. L. Mao, Phys. Rev. B **89**, 180102 (2014).

[37] Y. Zhang, Y. Li, Y. Ma, Y. Li, G. Li, X. Shao, H. Wang, T. Cui, X. Wang, and P. Zhu, Sci. Rep. **5**, 14681 (2015).

[38] The topological semimetal here refers to a semimetal with nontrivial $\mathbb{Z}_2$ topology, which is different from the Weyl or Dirac semimetals where band touchings only occur at a few isolated points in the Brillouin zone.

[39] A. Jain, S. P. Ong, G. Hautier, W. Chen, W. D. Richards, S. Dacek, S. Cholia, D. Gunter, D. Skinner, G. Ceder, and K. A. Persson, APL Mater. **1**, 011002 (2013).

[40] J. P. Perdew, K. Burke, and M. Ernzerhof, Phys. Rev. Lett. **77**, 3865 (1996).

[41] G. Kresse and J. Furthmüller, Comput. Mater. Sci. **6**, 15 (1996).

[42] N. Marzari and D. Vanderbilt, Phys. Rev. B **56**, 12847 (1997); I. Souza, N. Marzari, and D. Vanderbilt, *ibid.* **65**, 035109 (2001).

[43] A. A. Mostofi, J. R. Yates, Y.-S. Lee, I. Souza, D. Vanderbilt, and N. Marzari, Comput. Phys. Commun. **178**, 685 (2008).

[44] H. Huang, Z. Liu, H. Zhang, W. Duan, and D. Vanderbilt, Phys. Rev. B **92**, 161115 (2015).

[45] H. Huang, S. Zhou, and W. Duan, Phys. Rev. B **94**, 121117 (2016).

[46] H. Huang and F. Liu, Phys. Rev. B **95**, 201101 (2017).

[47] M. P. López Sancho, J. M. López Sancho, and J. Rubio, J. Phys. F **14**, 1205 (1984); **15**, 851 (1985).

[48] H. Huang, J. Liu, and W. Duan, Phys. Rev. B **90**, 195105 (2014).

[49] H. Huang, Z. Wang, N. Luo, Z. Liu, R. Lü, J. Wu, and W. Duan, Phys. Rev. B **92**, 075138 (2015).

[50] Q. Wu, S. Zhang, H.-F. Song, M. Troyer, and A. A. Soluyanov, arXiv:1703.07789.

[51] R. Yu, X. L. Qi, A. Bernevig, Z. Fang, and X. Dai, Phys. Rev. B **84**, 075119 (2011).

[52] A. A. Soluyanov and D. Vanderbilt, Phys. Rev. B **83**, 235401 (2011).

[53] M. Taherinejad, K. F. Garrity, and D. Vanderbilt, Phys. Rev. B **89**, 115102 (2014).

[54] H. Huang, J. Liu, D. Vanderbilt, and W. Duan, Phys. Rev. B **93**, 201114 (2016).

[55] N. B. Kopnin, T. T. Heikkilä, and G. E. Volovik, Phys. Rev. B **83**, 220503 (2011).

[56] G. Volovik, J. Supercond. Novel Magn. **26**, 2887 (2013).

[57] G. Volovik, Phys. Scr. **T164**, 014014 (2015).

[58] T. T. Heikkilä and G. E. Volovik, *Basic Physics of Functionalized Graphite* (Springer, Cham, Switzerland, 2016), pp. 123–143.

[59] A. Yamakage, Y. Yamakawa, Y. Tanaka, and Y. Okamoto, J. Phys. Soc. Jpn. **85**, 013708 (2015).

[60] Z. Zhu, M. Li, and J. Li, Phys. Rev. B **94**, 155121 (2016).

[61] Y. Chen, Y.-M. Lu, and H.-Y. Kee, Nat. Commun. **6**, 6593 (2015).

[62] G. Bian, T.-R. Chang, R. Sankar, S.-Y. Xu, H. Zheng, T. Neupert, C.-K. Chiu, S.-M. Huang, G. Chang, I. Belopolski *et al.*, Nat. Commun. **7**, 10556 (2016).

[63] G. Bian, T.-R. Chang, H. Zheng, S. Velury, S.-Y. Xu, T. Neupert, C.-K. Chiu, S.-M. Huang, D. S. Sanchez, I. Belopolski, N. Alidoust, P.-J. Chen, G. Chang, A. Bansil, H.-T. Jeng, H. Lin, and M. Z. Hasan, Phys. Rev. B **93**, 121113 (2016).